Bioactive Materials 9 (2022) 183–197

Contents lists available at ScienceDirect

Bioactive Materials

journal homepage: www.sciencedirect.com/journal/bioactive-materials

Engineered neutrophil apoptotic bodies ameliorate myocardial infarction by promoting macrophage efferocytosis and inflammation resolution

Lili Bao [a,1], Geng Dou [a,1], Ran Tian [b,1], Yajie Lv [c], Feng Ding [a], Siying Liu [a], Ruifeng Zhao [d], Lu Zhao [e], Jun Zhou [a], Lin Weng [b], Yan Dong [a], Bei Li [a], Shiyu Liu [a,***], Xin Chen [b,**], Yan Jin [a,*]

[a] State Key Laboratory of Military Stomatology & National Clinical Research Center for Oral Diseases & Shaanxi International Joint Research Center for Oral Diseases, Center for Tissue Engineering, School of Stomatology, The Fourth Military Medical University, Xi'an, 710032, China
[b] School of Chemical Engineering and Technology, Shaanxi Key Laboratory of Energy Chemical Process Intensification, Institute of Polymer Science in Chemical Engineering, Xi'an Jiao Tong University, Xi'an, 710049, China
[c] Department of Dermatology, Tangdu Hospital, The Fourth Military Medical University, Xi'an, 710038, China
[d] State Key Laboratory of Military Stomatology & National Clinical Research Center for Oral Diseases & Shaanxi International Joint Research Center for Oral Diseases, Center for Digital Dentistry, School of Stomatology, The Fourth Military Medical University, Xi'an, Shaanxi, 710032, China
[e] State Key Laboratory of Military Stomatology & National Clinical Research Center for Oral Diseases & Shaanxi Clinical Research Center for Oral Diseases, Department of Oral and Maxillofacial Surgery, School of Stomatology, The Fourth Military Medical University, Xi'an, Shaanxi, 710032, China

ARTICLE INFO

Keywords:
Neutrophils
Apoptotic bodies
Engineering
Inflammation
Myocardial infarction

ABSTRACT

Inflammatory response plays a critical role in myocardial infarction (MI) repair. The neutrophil apoptosis and subsequent macrophage ingestion can result in inflammation resolution and initiate regeneration, while the therapeutic strategy that simulates and enhances this natural process has not been established. Here, we constructed engineered neutrophil apoptotic bodies (eNABs) to simulate natural neutrophil apoptosis, which regulated inflammation response and enhanced MI repair. The eNABs were fabricated by combining natural neutrophil apoptotic body membrane which has excellent inflammation-tropism and immunoregulatory properties, and mesoporous silica nanoparticles loaded with hexyl 5-aminolevulinate hydrochloride (HAL). The eNABs actively targeted to macrophages and the encapsulated HAL simultaneously initiated the biosynthesis pathway of heme to produce anti-inflammatory bilirubin after intracellular release, thereby further enhancing the anti-inflammation effects. In *in vivo* studies, the eNABs efficiently modulated inflammation responses in the infarcted region to ameliorate cardiac function. This study demonstrates an effective biomimetic construction strategy to regulate macrophage functions for MI repair.

1. Introduction

Myocardial infarction (MI) is a worldwide leading cause of death and disability which still requires efficient therapy [1]. Following MI, tremendous neutrophils, monocytes and macrophages are recruited to the injured myocardium to induce inflammation response [2,3]. The persistent infiltration of these inflammatory cells led to delayed inflammation resolution and hindered tissue repair, which further resulted in adverse remodeling and impaired cardiac function [4]. Natural resolution is initiated when neutrophils underwent apoptosis and subsequently were ingested by macrophages in the inflammatory zone [5]. The efferocytosis switched the macrophage phenotype and elevated the secretion of anti-inflammatory factors to promote tissue homeostasis, resulting in inflammation resolution [6,7]. Simultaneously, apoptotic neutrophils secreted mediators like annexin A1 and lactoferrin that inhibited further neutrophil recruitment [8–10]. Thus, the precise modulation and induction of endogenous neutrophil apoptosis could be potentially beneficial to promote regeneration [11,12]. However, the intrinsic survival/apoptosis balance in neutrophils is monitored by an intricate network of signaling factors, and treatment

Peer review under responsibility of KeAi Communications Co., Ltd.
* Corresponding author.
** Corresponding author.
*** Corresponding author.
E-mail addresses: liushiyu@vip.163.com (S. Liu), chenx2015@xjtu.edu.cn (X. Chen), yanjin@fmmu.edu.cn (Y. Jin).
[1] These authors contributed equally to this work.

https://doi.org/10.1016/j.bioactmat.2021.08.008
Received 8 May 2021; Received in revised form 4 August 2021; Accepted 5 August 2021
Available online 27 August 2021

that induces neutrophil apoptosis may disturb the innate immune response [13]. Moreover, it is difficult to precisely realize the induction of neutrophils apoptosis *in situ*. Consequently, alternative therapeutic approaches that supply apoptotic neutrophils to overcome complicated inflammatory microenvironment seem attractive for effective myocardial infarction treatment.

Although the supply of apoptotic neutrophils opened a window for MI treatment, direct engraftment of exogenous apoptotic cells may be associated with inflammation owing to the accompanying cell debris or inflammatory products. Apoptotic cells can also facilitate intercellular communication through the release of extracellular vesicles (EVs) such as apoptotic bodies (ABs), which inherit surface signal molecules from their source cells and can initiate macrophage polarization and inflammation resolution. Therefore, ABs have stoked great interest as therapeutic vehicles to coordinate important stages of the immune response [14]. Moreover, the large-scale production, appropriately stability, smaller size, and readily accessibility endow ABs distinct advantages in treatment from a clinical standpoint compared with cell-based therapy [15]. Our previous studies have demonstrated the regeneration capacity of ABs in maintaining tissue homeostasis and modulating inflammation [16–18]. Nevertheless, several challenges need to be addressed before clinical translation, including the inherent heterogeneity of ABs, complex content and the whole-body distribution after systemic administration. Naïve EVs can effectively overcome these bottlenecks through engineering modification to improve their tissue-specific targeting and functional specialization, ultimately achieving definite therapeutic effects especially for cardiac regenerative medicine [19–21].

In the present study, we have developed engineered neutrophil apoptotic bodies (denoted 'eNABs') to mimic the role of apoptotic neutrophils to reprogram macrophages and resolve inflammation after MI (Scheme 1). The eNABs were constructed by fusing the natural membrane of neutrophil apoptotic bodies with hexyl 5-aminolevulinate hydrochloride (HAL) preloaded mesoporous silica nanoparticles (MSN^{HAL}), which inherited the proteomics of apoptotic neutrophil membrane with the inflammation-tropism and immunoregulatory effects. Moreover, the original heterogenous contents of ABs were replaced with MSN^{HAL}. The encapsulated HAL would initiate the biosynthesis pathway of heme to generate extra anti-inflammatory bilirubin to enhance the immunoregulatory effect after intracellular release [22], which was achieved by the introduction of an esterase-degradable polyester cap on the surface of MSNs. The resulting eNABs could effectively reprogram macrophages function in the infarcted zone to modulate the inflammation for tissue regeneration, which demonstrated a high therapeutic efficacy in rat MI models.

2. Materials and methods

2.1. Animals

All rats used in this study were purchased from Animal Center of the Fourth Military Medical University. All experimental procedures were approved by the Fourth Military Medical University and were performed according to the Guidelines of Intramural Animal Use and Care Committee of the Fourth Military Medical University.

2.2. Cell culture

Bone marrow-derived neutrophils were obtained by the commercial kit (TBD2013NR, TBD, China). Briefly, the rats were euthanized and the femurs and tibias were dissected from the rats. The bone marrow was rinsed with the rinsing buffer and filtered through a 70-μm cell strainer to generate the single-cell suspension. The neutrophils were isolated from the suspension by the density gradient centrifugation. Neutrophils were maintained in the RPMI-1640 medium supplemented with 10% fetal bovine serum (FBS).

Bone marrow-derived macrophages were maintained in DMEM (High glucose) supplemented with 10% FBS. The femurs and tibias were dissected from the rats and the bone marrow was rinsed with cold PBS to generate the single-cell suspension. Followed by erythrocyte lysis, the cells were concentrated and resuspended in complete media with M-CSF (20 ng/ml) to induce the maturation of macrophages for 7 days.

Rat myocardial cell line H9C2 was obtained from American Type Culture Collection and maintained in DMEM (High glucose) supplemented with 10% FBS. All cells were incubated in a humidified

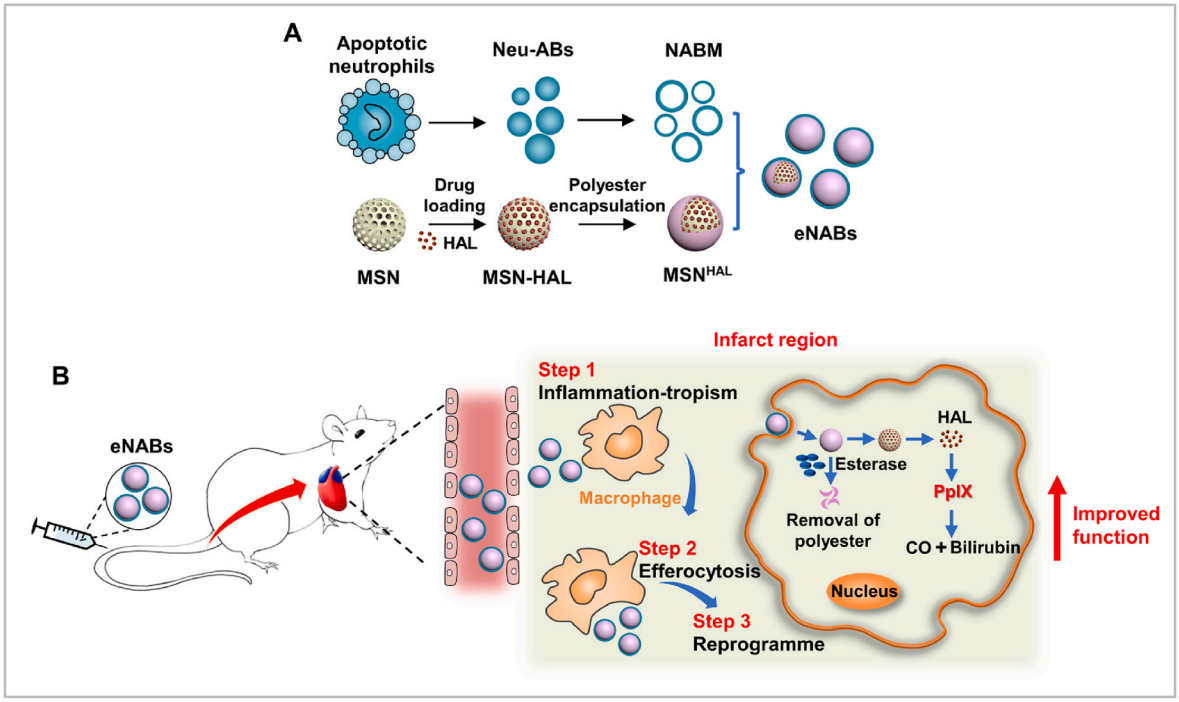

Scheme 1. Schematic of engineered neutrophil apoptotic bodies (eNABs) for MI treatment. (**A**) Scheme of the eNABs fabrication. (**B**) Illustration of eNABs therapy for inflammatory regulation in a rat MI model.

atmosphere with 5% CO_2 at 37 °C (Thermo Fisher Scientific). The media were refreshed every third day, and the cells were passaged once they reached 70–80% confluence.

The Neutrophils and BMDMs were collected by centrifugation at 800 rpm for 5 min, and then the cells were characterized by flow cytometry (Beckman Coulter, USA) and fluorescence staining.

2.3. Neutrophil derived apoptotic bodies collection and characterization

Neutrophils were treated with staurosporine at 0.5 μM for 3 h to induce apoptosis *in vitro*. The culture media were collected to isolate the Neu-ABs. Briefly, the media were centrifuged at 50 g for 5 min to remove the cells and debris for twice. Then, the supernatant was further centrifuged at 1000 g for 10 min to pellet the ABs. The concentrated ABs were resuspended in PBS and quantified by the BCA protein assay kit.

The morphology and size of ABs were detected by SEM (Hitachi, Japan) and DLS analysis (Malvern, UK). Fluorescence staining and flow cytometry analysis of ABs was conducted using an Annexin V-FITC apoptosis assay kit (A005-2, 7 Sea Biotech, China) and *anti*-C1q antibody (CL7501F, CEDARLANE). Western blotting was performed to characterize the protein constitution of the ABs.

2.4. Preparation and characterization of MSNs

MSN was prepared by the classic CTAB template, base-catalyzed sol-gel method according to previous work [23]. Firstly, the pH of 1000 ml of deionized water was adjusted to approximately 11 using 52.8 ml of ammonium hydroxide (25–28 wt% $NH_3{\cdot}H_2O$). Then, the temperature was increased to 323 K. 1.12 g of CTAB was added and completely dissolved. After that, 5.8 ml of tetraethyl orthosilicate (TEOS) is added dropwise with stirring rapidly. After 2 h stirring, the mixture was incubated overnight, centrifuged, and washed thoroughly with distilled water and ethanol. The synthesized silica nanoparticles were dispersed in ethanol for 30 min by ultrasonic treatment, and then a 1:1 (v/v) mixture of 20 ml of water and 1,3,5-trimethylbenzene was added. The mixture was placed in an autoclave and kept at 140 °C for 4 days without stirring. The resulting white powder was washed five times with ethanol and water, respectively. Then, the surfactant template was removed by extraction with acidic methanol (9 ml HCl/400 ml methanol, 36 h) at 70 °C. The resulting MSNs were centrifuged, washed with ethanol several times, and dried under vacuum for 20 h.

2.5. Fabrication, characterization and in vitro drug release of MSN^{HAL}

Firstly, 10 mg MSN, 1 mg hexyl 5-aminolevulinate hydrochloride (HAL) and 10 μl glycerol dimethacrylate (GDMA) were completely dispersed in 50 μl water by ultrasonic treatment for 20 min (100 W). The mixture was placed in a vacuum oven and repeat vacuum (−1 bar) 3 times for 10 min each to generate HAL and GDMA co-loaded MSN^{HAL}. At the same time, 24 mg APS was dissolved in 3 ml water and deoxidized for 20 min under nitrogen, 80 μl TEMED was dissolved in 800 μl water. After that, 2500 μl of APS solution and 440 μl of TEMED solution were mixed with HAL and GDMA co-loaded MSN^{HAL}. The free radical polymerization was performed at room temperature under nitrogen to form polymerized glyceryl dimethacrylate (PGDMA) cap to prevent HAL from leaking. The solution was stirred at room temperature under nitrogen for 1 h to complete polymerization. The resulting nanoparticles were washed with water and dried in a vacuum oven at 37 °C overnight. The loading efficiency of MSN to HAL was calculated as follows.

$$Loading\ efficiency = \frac{Weight\ of\ drug\ in\ MSNs}{Initial\ weight\ of\ drug}$$

The MSN and MSNs-polyester before and after degradation by esterase were observed by TEM. Quantitative analysis (TGA) of these samples (STA449F5, NETZSCH) was also performed. The pore size of these samples was measured by a surface area and porosity analyzer (V-Sorb 4800, Gold APP). The *in vitro* drug release process was determined by the fluorescence intensity change of the solution against incubation time, which was detected by a fluorescence spectrophotometer (Guangdong F-280, China). The rhodamine (RhB) was selected as a model drug to replace HAL in this experiment due to its strong fluorescence for easy detection. Specifically, 10 mg of $MSNs^{RhB}$ was dispersed in 10 ml of two different phosphate buffer solutions (a: PBS with esterase; b: PBS without esterase) under shaking at 37 °C. Then the supernatant was collected by centrifugation at different timepoints. The fluorescence intensity of the supernatant was tested to monitor the *in vitro* drug release.

2.6. Fabrication and characterization of engineered neutrophil apoptotic bodies

Firstly, the neutrophils apoptotic body membrane was collected by removal of the vesicle components of ABs through hypotonic treatment and sonication. The ABs were resuspended in 0.25 × PBS at 4 °C for 2 h, followed by sonication for 5 s (VCX 130 PB, Sonics, USA). After washing with the double distilled water (ddH_2O) for twice, the membrane was concentrated by centrifugation at 5000*g* for 10 min. Then, the membrane suspensions were subjected to 10-circle extrusion through 400 nm polycarbonate membranes to product the final NABM. Finally, the mixture of NABM and MSNs were co-extruded through the 200 nm polycarbonate membranes for at least 10 cycles. The resulted eNABs were obtained by centrifugation at 5000*g* for 10 min. The size and morphology of eNABs were detected by TEM (TECNAI Spirit, FEI) and DLS analysis (Malvern, UK). The membrane protein retention of the eNABs was confirmed by the Coomassie blue staining (P0017, Beyotime) and Western blotting. The membrane coating percentage was quantified by the detection of the fluorescence intensity. PKH67-labeled NABM were mixed with MSNs, followed by co-extrusion to generate eNABs. The fluorescence intensity in the NABM suspensions in the beginning and in the supernatant after eNABs concentration was detected using a multimode plate reader (HH3400, PerkinElmer) (excitation = 496 nm/emission = 520 nm). To assess the storage stability, MSNs and eNABs were resuspended in water and PBS, respectively for total 7 days to measure the size change by DLS. To evaluate the serum stability, eNABs and MSNs were resuspended in 100% serum for 4 h and the absorbance at 560 nm was measured using the multiplate reader (Epoch, BioTek, USA), water as the control.

The blood biocompatibility test was conducted to test the hemolysis index. Briefly, different concentrations of eNABs were added to the RBC suspensions in the final of 0.5 ml PBS solution. After incubation for 24 h, the samples were centrifugated at 4000 rpm for 5 min. The supernatants were collected to perform the UV–Vis analysis. The equal amounts of RBCs resuspended in 0.5 ml of PBS or water was used as negative control or positive control, respectively.

To monitor the pharmacokinetics of nanoparticles, DiR-labeled eNABs (2 mg particles per kg body weight) were injected into rats *via* the tail vein. At pre-determined time points (n = 3), whole blood samples were collected, and centrifuged at 3000 rpm for 10 min to remove the blood cells. The fluorescence intensities of the samples were measured for a quantitative analysis of eNABs in blood.

2.7. Western blot analysis

At first, the cell or tissue protein were extracted using the RIPA lysis buffer (P0013B, Beyotime). The protein concentration was determined by the BCA protein assay kit. All samples were prepared at a final concentration of 1 μg/μl in loading buffer (CW0027S, CwBio). Protein samples (20 μg) were loaded into a 10–15% SDS-polyacrylamide gel in the Bio-Rad Electrophoresis System to separate the proteins with different molecular weight. Then, the proteins in the gel were transferred to polyvinylidene difluoride (PVDF) membranes. After blocking in 5% bovine serum albumin (BSA) solution, the membranes were

incubated with primary antibodies (Integrin-α_L, ab186873, Abcam; Integrin-β_2, ab131044, Abcam; C1q, ab71940, Abcam; Integrin-β_3, ab75872, Abcam; CD11b, ab133357, Abcam; CD45, ab10558, Abcam; cleaved caspase-3, #9661s, Cell signaling technology; CD44, ab189524, Abcam; HO-1, ab68477, Abcam; β-tubulin, CW0098, CwBio; iNOS, ab15323, Abcam; CD206, ab125028, Abcam; Arginase-1, 93668s, Cell signaling technology; Histone H3, #9715, Cell signaling technology; GM130, 610,822, BD Biosciences) at 4 °C overnight. After incubation with the corresponding secondary antibodies, the PVDF membranes were imaged using Western chemiluminescent horseradish peroxidase (HRP) substrate (Millipore) with an imaging system (Tanon 4600, Shanghai).

2.8. Immunocytochemistry

The cells were cultured on slides or glass bottom cell culture dish. After different treatments, the cells were fixed with 4% PFA at 4 °C overnight, and permeated with 0.1% Triton X-100 for 15 min. After blocking with normal goat serum (37 °C, 1 h), the cells were stained with the primary antibodies (CD68, sc-9139, Santa Cruz Biotechnology; His48, ab33760, Abcam; CD11 b/c, ab1211, Abcam; F4/80, ab16911, Abcam; P-selectin, 3633 R, BioVision; ICAM-1, ab171123, Abcam; HO-1, ab68477, Abcam; iNOS, ab15323, Abcam; CD206, ab125028, Abcam; cardiac troponin T, ab8295, Abcam) at 4 °C overnight. After washing with PBS for three times, the cells were incubated with the appropriate fluorescence conjugated antibody at 37 °C for 1 h. Finally, the cells were counterstained with Hoechst 33,342 and imaged by the confocal microscope (Nikon, Japan). Intracellular reactive oxygen species was detected by the DCFH-DA probe (S0033S, Beyotime).

2.9. ELISA

In the *in vitro* immunoregulatory experiments, macrophages were treated with different formulations (25 μg/ml) for 24 h after pre-stimulation with LPS (1 μg/ml). The immune factors (TNF-α, IL-6, TGF-β, and IL-10) secreted by the macrophages from different groups were detected by the enzyme-linked immunosorbent assay kit according to the manufacturer's recommended protocol (NeoBioscience, China).

2.10. Rat model of myocardial infarction

Sprague Dawley female rats (10 weeks old) were subjected to a permanent ligation of the left anterior descending artery to induce MI, as previously described [24]. Briefly, rats were anesthetized and ventilated with a rodent respirator ventilator. The chest cavity and pericardium were opened to expose the heart, the left anterior descending (LAD) was ligated with a 7-0 silk suture, the chest was closed and the respirator was kept on to ventilate until the rats woke up.

The rat cardiac function was evaluated using a high-resolution echocardiography imaging system (VINNO X10-23 L, VINNO Technology). Two-dimensionally echocardiographic views of the long axis were obtained at the level of the papillary muscle. The left ventricular ejection fraction (LVEF) and fractional shortening (LVFS) were measured at the designated time points.

2.11. Targeting ability of eNABs in vivo

In a rat MI model, the near-infrared dye 1,1′-dioctadecyl-3,3,3′,3′-tetramethylindotricarbocyanine iodide (DiR) were used for *in vivo* tracking. DiR-labeled MSN^{HAL} or $eNAB^{HAL}$ (2 mg particles per kg body weight in 500 μl PBS) were intravenously infused through the tail veins. Rats treated with saline were used as controls. The rats were then euthanized 3, 12, 24 h after injection, the major organs were excised and monitored by an IVIS imaging system (Xenogen). To further quantify the targeting efficiency, hearts were harvested at 3,12 or 24 h post injection, weighed and homogenized, and fluorescence of the samples was measured. All tissue fluorescence values were normalized on the fluorescence intensity of the total injection dose. To further confirm the distribution of $eNAB^{HAL}$, the heart cryosections were stained with Hoechst 33,342. Images were taken using a confocal microscope (Olympus, FV1000s).

2.12. Therapeutic evaluation in MI model rats

In a rat MI model, PBS, $eNAB^{null}$, MSN^{HAL} or $eNAB^{HAL}$ (2 mg per kg body weight in 500 μl PBS) was intravenously infused through the tail veins. After the echocardiography session at 4 weeks, animals were euthanized and the hearts were collected for histological studies. Experiments related to the collection of heart sections and echocardiography data were performed blinded to the preparation of the rats for the experiments.

2.13. Toxicity evaluation

Rats were intravenously administered with $eNAB^{null}$, MSN^{HAL} or $eNAB^{HAL}$ (2 mg per kg body weight in 500 μl PBS), rats treated with saline were used as controls. After 4 weeks, the blood was collected and centrifuged at 3000 rpm for 10 min. Finally, the rats were euthanized. Major organs, including the heart, liver, spleen, lung and kidney were excised and used for hematoxylin and eosin (H&E) staining. Clinical serum biochemistry analysis was also analyzed by automated Chemistry analyzer (Chemray 800, Rayto Life and Analytical Sciences Co., Ltd.). The *in vitro* cytotoxicity evaluation was performed by incubation of macrophages with different concentrations of eNABs for 24 h. Then the cell viability was detected by CCK8 kit (40203ES60, Yeasen).

2.14. Histology and immunofluorescence in vivo

The rat hearts were fixed in 4% PFA for a minimum of 24 h. The fixed tissues were embedded in paraffin and sectioned for H&E and Masson's trichrome staining. Masson's trichrome staining was performed to evaluate fibrotic tissue formation after infarction according to the manufacturer's instructions (BA4079A, Baso diagnostics). Images were captured using a microscope, the percentage of macrophages infiltrated area in the border zone and infarct size was quantified using Image J.

For immunofluorescence, OCT-embedded tissue sections were fixed with 4% PFA and stained with primary antibodies for confocal microscopy (CD11 b/c, ab1211, Abcam; CD68, sc-9139, Santa Cruz Biotechnology; His48, ab33760, Abcam; CD3, sc-20047, Santa Cruz Biotechnology; iNOS, ab15323, Abcam; CD206, ab125028, Abcam; CD31, ab119339, Abcam) at 4 °C overnight, followed by treatment with the appropriate secondary antibody (Alexa Fluor 488 AffiniPure goat anti-mouse IgG (H + L), 33206ES60, Yeasen; Cy™3 AffiniPure Goat Anti-Rabbit IgG (H + L), 33108ES60, Yeasen; Fluorescein (FITC) AffiniPure Goat Anti-Rabbit IgG (H + L), 33107ES60, Yeasen) for 2 h at room temperature. Finally, cell nuclei were counterstained with Hoechst 33,342 (Sigma-Aldrich). Images were obtained using Olympus laser-scanning confocal microscope and quantified using Image J.

2.15. Statistical analysis

All data were expressed as means ± standard deviation (SD). Statistical comparisons between data sets were made with analysis of normality and variance, followed by a two-tailed unpaired Student's t-test for comparing differences between two groups, and one-way ANOVA test for multiple groups. Tukey or Dunnett's T3 correction was used when multiple comparisons were performed. All statistical analysis was completed using the SPSS 19.0 software (Chicago, IL). Differences were considered statistically significant when $P < 0.05$.

3. Results

3.1. Construction and characterization of Neu-ABs and eNABs

To fabricate the engineered neutrophil apoptotic bodies, which are able to simulate the apoptosis of neutrophils and the ensuing biological function *in vivo*, we first isolated and purified the neutrophils derived from bone marrow by the gradient separation method (Fig. S1A). Fluorescence images and flow cytometry analysis demonstrated high CD45 and His48 expression levels in neutrophils (Figs. S1B–C). The Wright's staining was further performed to identify neutrophils (Fig. S1D). As shown in Fig. 1A, neutrophils derived apoptotic bodies (Neu-ABs) were isolated from apoptotic neutrophils as previously described [18], and neutrophil derived apoptotic body membranes (NABM) were then processed for eNABs preparation. The abbreviations of other nanoparticles or engineered nanovesicles mentioned in this paper were also listed in Table 1. The final engineered nanovesicles (eNABs) were prepared by fusing NABM with MSN^{HAL} cores *via* co-extrusion through 200 nm polycarbonate membrane. Scanning electron microscope (SEM) imaging (Fig. 1B) and dynamic light scattering (DLS, Fig. S2A) presented the morphology and size distribution of Neu-ABs. The expression of Annexin V and C1q were further detected by fluorescence staining and flow cytometry analysis (Fig. 1C and Fig. S2B). Western blotting analysis were performed on a series of membrane and intracellular protein markers (Fig. 1D). Neu-ABs exhibited similar expressions of lymphocyte function-associated antigen-1 (LFA-1, $\alpha_L\beta_2$-integrin) [25], CD11b and CD45 compared with neutrophil, and notably higher expression of cleaved caspase-3, which indicated the successful apoptosis induction.

The vesicle components should be removed adequately for the preparation of NABM. After hypotonic treatment and sonication, the components were hardly found in the PKH67-NABM indicated by the Hoechst staining (Fig. S2C). Besides, there is no obvious expression of Histone H3 (the protein component of chromatin), and GM130 (the matrix protein of cis-Golgi apparatus) in the final NABM (Fig. S2D). The successful membrane coating of NABM on MSN was visualized using transmission electron microscopy (TEM) (Fig. 1E). As can be seen from this figure, the final eNABs exhibited a spherical morphology with obvious organic membrane surrounding MSN cores. More information was provided by dynamic light scattering (DLS) (Fig. 1F–G) and zeta potential measurements (Fig. 1H), which demonstrated 20 nm size increase and surface charge change to the approximate level of NABM after membrane coating. These results clearly indicated the shielding of MSN cores with NABM. Fluorescent imaging showed an overlap of PKH67 (green) and RhB (red) fluorescence, further confirming the successful NABM coating on MSNs (Fig. 1I). Incorporation of the intrinsic membrane proteins within the outer membrane bilayers of eNABs was then examined by sodium dodecyl sulfate polyacrylamide gel electrophoresis (SDS-PAGE) and Western blotting. As shown in Fig. 1J–K, eNABs exhibited similar total protein profile compared with NABM, and the expressions of main surface antigens, including LFA-1 ($\alpha_L\beta_2$-integrin), C1q, Integrin-β3, CD11b and CD45, were also confirmed. These results demonstrated that eNABs inherited the surface antigen expressions of NABM, which will own the comparable biological functions with apoptotic neutrophils.

The membrane coating efficiency was determined to be approximately 96% (Fig. S2E) according to the fluorescence signal change of free NABM before and after coating process. The storage stability of eNABs in various dispersion medium was also investigated, which displayed a constant size in either water or phosphate buffered saline (PBS) over 7 days. However, MSNs immediately aggregated right after dispersing in PBS and showed a significant increase in size during storage (Fig. 1L). In addition, serum stability (Fig. 1M) and blood compatibility (Fig. S2F) were also detected to evaluate the *in vivo* performance of eNABs. The much lower absorbance change of eNABs in serum than that of MSNs indicated the high serum stability of eNABs, and no visible hemolysis even with high concentration of eNABs up to 1000 μg/ml indicated the high blood compatibility of eNABs. Furthermore, the stability of eNABs in circulation following injection (Fig. S2G) showed that the blood elimination half-life ($t_{1/2}$) of eNABs is about 2 h, and this circulation time is sufficient for the targeted enrichment of eNABs to the MI region. Moreover, eNABs have no significant cytotoxicity on macrophages (Fig. S2H). These characterization results indicated that the engineered ABs were successfully generated with well-defined size, similar proteomic profile of Neu-ABs and excellent biological performance.

3.2. Specific inflammation targeting and selective cellular uptake

The membrane proteins on neutrophils, including CD44, CD11b and LFA-1 ($\alpha_L\beta_2$-integrin), were closely associated with the recognition of inflamed endothelium during leukocyte migration, adhesion and homing [26]. High expression of these surface receptors in membrane would enhance the homing affinities to the inflamed tissues. Western blotting confirmed the markedly enhanced expression of these adhesion molecules in LPS-stimulated neutrophils and Neu-ABs compared to untreated groups (Fig. 2A). The presence and enrichment of adhesion molecules on eNABs were further examined, confirming the successful transfer of surface proteins to the shell of eNABs (Fig. 2B). To investigate the specific adhesion of eNABs to inflamed tissues *in vitro*, human umbilical vascular endothelial cells (HUVECs) were treated with TNF-α to simulate the inflamed endothelium. The activation of HUVECs were validated by the enhanced fluorescence intensity of P-selectin and ICAM-1 (green), which is responsive for the leukocyte recruitment and adhesion. At the same time, significant red fluorescence was observed in cells incubated with eNABs, but not in those incubated with MSNs (Fig. 2C–D), demonstrating the inflammation-targeting ability of eNABs due to the NABM-mediated adhesive interactions. Therefore, the binding affinity of eNABs to inflamed endothelium is speculatively conferred by the considerable levels of existing adhesion molecules on the neutrophil membrane.

To determine the selective cellular targeting ability, the intracellular uptake of eNABs by macrophages (target cells) and cardiomyocytes (control cells) was firstly studied. Expression of CD68, CD11b and F4/80 in bone marrow derived macrophages (BMDMs) were confirmed by fluorescence images and flow cytometry analysis (Figs. S1E–F). The fluorescent images in Fig. 2E showed that RhB-eNABs were extensively internalized by macrophages (white), whereas negligible nanoparticles were observed in cocultured cardiomyocytes (green), indicating the specific uptake of eNABs by macrophages under the simulated cardiac microenvironment *in vitro*. The results were also confirmed *via* incubating eNABs with macrophages or H9C2 respectively, implying the preferred uptake of eNABs by macrophages (Figs. S3A–B). In addition, Z-stack fluorescence imaging visualized the red signals of eNABs within the cytoplasma, indicating the intracellular uptake of eNABs by macrophages (Fig. 2F). Moreover, the time-dependent and concentration-dependent uptake of eNABs by macrophages were detected by fluorescence images (Figs. S3C–D) and flow cytometry analysis (Figs. S3E–F), demonstrating the autonomous engulfment of eNABs by macrophages. Furthermore, we added the different agents to the macrophages to confirm the specific uptake (Fig. 2G). NABM and eNABs showed similar high red fluorescence intensity in macrophages compared to MSNs group, revealing that the remarkably enhanced cellular uptake of eNABs by macrophages owing to the apoptotic membrane on the outer shell. Altogether, these results suggested the excellent targeted capacity of eNABs to inflamed tissues and the specific uptake by macrophages as we have designed it. Considering the inflammatory microenvironment in the injured myocardial area after MI, eNABs should be reasonably applied to the targeted therapy for MI.

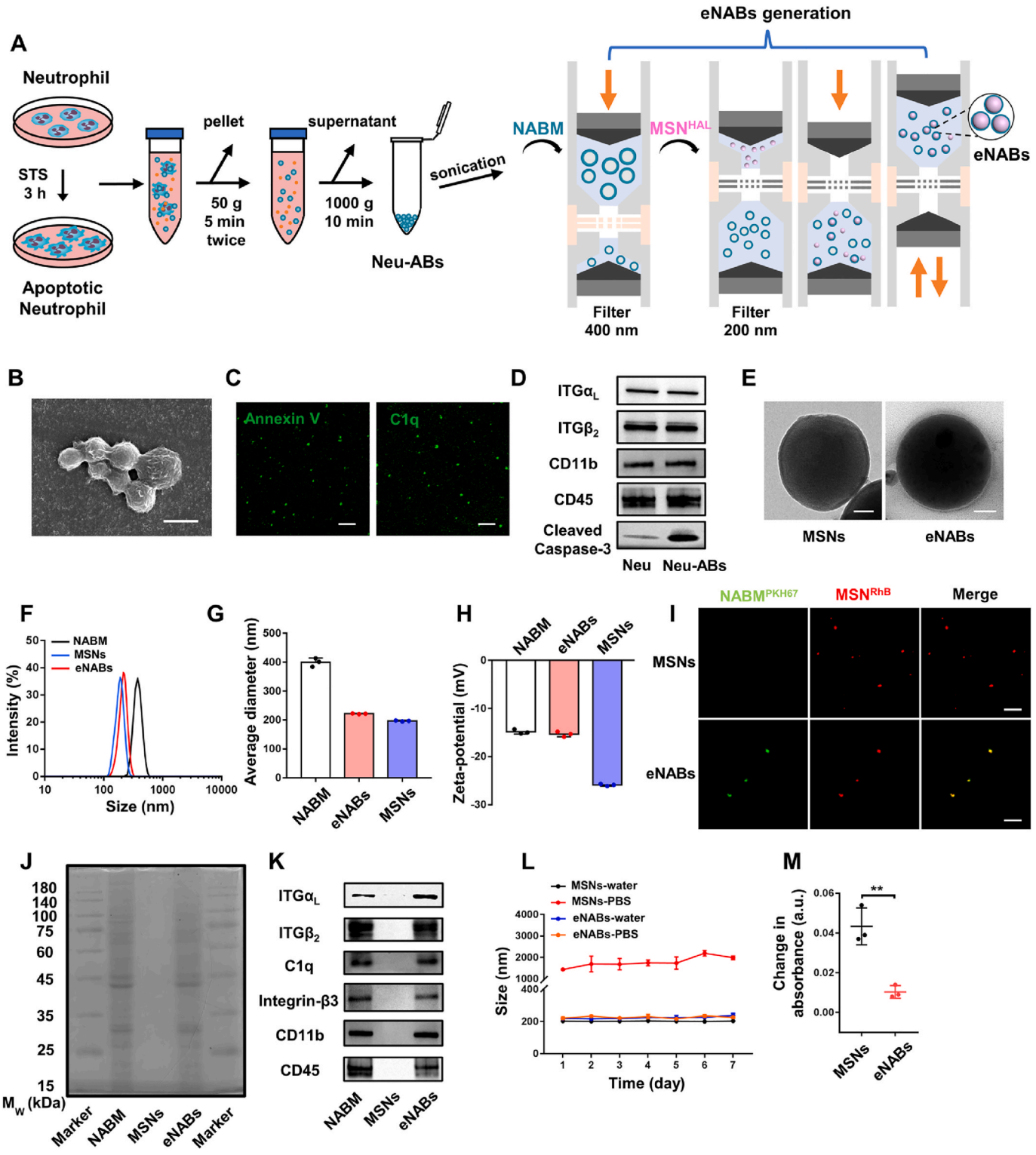

Fig. 1. Preparation and characterization of Neu-ABs and eNABs. (**A**) Schematic shows the purification of Neu-ABs through apoptosis induction and serial centrifugations, as well as the generation of eNABs. The latter process was conducted using a liposome extruder and followed two steps: (i) NABM was generated by repeated extrusion through the first filter (pore diameter: 400 nm); (ii) eNABs were generated through repeated extrusion of the mixed suspension (NABM and MSNs) through a smaller filter (pore diameter: 200 nm). (**B**) Representative SEM image of ABs derived from neutrophils. Scale bars, 1 μm. (**C**) The Annexin V and C1q staining of Neu-ABs. Scale bars, 5 μm. (**D**) Western blotting analysis of neutrophil and Neu-ABs. (**E**) Representative TEM images of MSNs and eNABs. Scale bars, 50 nm. (**F**) Size distribution of NABM, MSNs, and eNABs measured by DLS. Average diameter (**G**) and surface zeta potential (**H**) of NABM, MSNs, and eNABs (n = 3). (**I**) Representative images of the fluorescence colocalization of PKH67-labeled NABM and rhodamine-labeled MSNs in eNABs. The pure rhodamine-labeled MSNs were used as a control. Scale bars, 10 μm. (**J**) SDS-PAGE protein analysis of NABM, MSNs, and eNABs with Coomassie Blue staining. (**K**) Western blot analysis for membrane-specific protein markers. The storage stability (**L**) and the serum stability (**M**) of eNABs (n = 3). Data are presented as means ± SD. Statistical analysis between two groups was performed using unpaired two-tailed t-tests for **M** (**$P < 0.01$).

Table 1
Abbreviation and composition used in this study.

Abbreviation	Composition	Loading cargos
Neu-ABs	Neutrophil derived apoptotic bodies	None
NABM	Neutrophil derived apoptotic body membranes	None
MSN	Mesoporous silica nanoparticle	None
MSN^{HAL}		HAL
$eNAB^{null}$	Engineered neutrophil apoptotic bodies	None
$eNAB^{HAL}$		HAL

3.3. Immunomodulatory effect generated from efferocytosis

The previous studies and our work have shown that ABs could elicit a considerable immunomodulatory effect on macrophages [18]. Except for the effect exerted by the content of ABs on the target cell, part of the effect is attributed to the efferocytosis process [5,17]. Therefore, we first comparatively evaluated the anti-inflammation effects of NABM, MSNs and eNABs. LPS-stimulated BMDMs were used to mimic the inflammatory cells *in vitro*, which exhibited the enhanced iNOS expression and elevated secretion of pro-inflammatory factors (Figs. S4A–C). After administration of NABM or eNABs, the population of iNOS-positive pro-inflammatory macrophages were notably reduced and CD206-positive anti-inflammatory macrophages were obviously increased indicated by fluorescent images (Fig. S4A). When the inflammatory macrophages switch to the anti-inflammatory phenotype, the activity of arginase-1 (Arg1) will increase obviously [27]. Western blotting analysis showed that the protein expression levels of iNOS, CD206 are in accordance with the fluorescence data, and intriguingly the Arg1 level was significantly increased after NABM and eNABs treatment (Fig. S4B). Inflammatory factors are the critical link in the homeostasis of microenvironment. Furthermore, as we expected, NABM and eNABs treatment notably decreased the secretion of pro-inflammatory cytokines (TNF-α, IL-6) by inflammatory macrophages, and promoted the secretion of anti-inflammatory cytokines (TGF-β, IL-10) (Fig. S4C). Taken together, these data suggest that eNABs could generate the anti-inflammatory effects caused by efferocytosis inherited from the Neu-ABs.

3.4. Construction and characterization of the intracellular drug delivery system

To further enhance the immunoregulatory ability of eNABs, we encapsulate hexyl 5-aminolevulinate hydrochloride (HAL) in these nanovesicles. The HAL is a therapeutic molecule approved by FDA, which initiated the biosynthesis and metabolism pathway of heme *in vivo* to generate the final anti-inflammatory products (CO and bilirubin). As to achieve precise treatment, the esterase-degradable polyester was employed as a cap to prevent the pre-release before internalization by target cells to realize the intracellular delivery [18,28]. The schematic design of HAL loading was summarized in Fig. 3A. After our calculation (Table S1), the drug-loading efficiency of MSNs reaches to 60.70% when the ratio of HAL to MSNs is 0.1/1, which demonstrates the excellent drug loading capacity of MSNs. Firstly, the morphology of MSNs as well as polyester-capped MSNs before and after esterase treatment was visualized using TEM (Fig. 3B). The obvious organic layer around MSNs can be observed after polymerization, which rapidly disappeared after co-incubation with esterase, indicating the formation and degradability of polyester cap as design. The formation and esterase-dependent degradation of polyester cap were further quantitatively investigated by thermogravimetric analysis (TGA) (Fig. 3C). As can be seen from this figure, approximately 4.94 wt% of polyester conjugated with MSNs, which could be majorly removed by esterase ending with a residual percentage about 0%. The esterase-triggered degradation of polyester cap re-opened the pores of MSNs (Fig. 3D), resulting in on-demand HAL release only in the presence of esterase (intracellular microenvironment of target cells) for precise treatment (Fig. 3E). Moreover, the HAL loading and polyester cap formation did not perform visible change of the morphology, size, surface charge and membrane coating percentage of eNABs (Figs. S5A–D), which demonstrated the successful introduction of additional intelligence drug delivery system without influence of the original functions of eNABs.

3.5. Enhanced anti-inflammation ability of $eNAB^{HAL}$ in vitro

After determination of the successful construction of the drug loading and release system, the anti-inflammation ability of eNABs encapsulated with HAL by promoting macrophage polarization to the anti-inflammatory state *in vitro* was studied with LPS-stimulated BMDMs. The intracellular delivery capability and detailed mechanism of $eNAB^{HAL}$ to enhance anti-inflammation effect was first tested, as shown in the schematic diagram (Fig. 4A). Once $eNAB^{HAL}$ were internalized by macrophages, the degradation of polyester by esterase will trigger the release of HAL, followed by subsequent synthesis of intermediate products protoporphyrin X (PpIX) with spontaneous fluorescence to permit the intracellular delivery. Then, biosynthesis and metabolism pathway of heme were initiated to produce anti-inflammatory bilirubin with the assistance of the heme oxygenase-1 (HO-1) (Fig. S6) [22]. Fluorescence imaging showed extensive red signals in inflammatory cells treated with $eNAB^{HAL}$ (Fig. 4B), indicating the successfully delivery of HAL in cells and the subsequent biosynthesis of PpIX. And the stronger red fluorescence intensity in $eNAB^{HAL}$ group than those in free HAL and MSN^{HAL} group demonstrated the specific delivery of HAL by eNABs to macrophages. The requisite enzyme HO-1 was detected by fluorescent images and western blots (Fig. 4C–D), the results revealed obvious HO-1 expression in HAL, MSN^{HAL} and $eNAB^{HAL}$-treated groups. To further confirm the production of the final catabolic metabolites, the synthesis level of bilirubin was measured by ELISA assay, $eNAB^{HAL}$-treated inflammatory cells secreted the most amounts of bilirubin (Fig. 4E). Altogether, these results demonstrated eNABs could facilitate the intracellular delivery of HAL to macrophages specifically.

Next, whether the intracellular HAL transferred by $eNAB^{HAL}$ enhanced the anti-inflammation ability was further validated in BMDMs stimulated by LPS. In general, the level of reactive oxygen species (ROS) in macrophages will be obviously increased under the inflammation state [29]. The generation of ROS was evaluated by the fluorescence probe DCFH-DA, and the results demonstrated obviously reduced ROS in $eNAB^{null}$, HAL, MSN^{HAL} and $eNAB^{HAL}$ treated groups (Fig. 4F). But the treatment of $eNAB^{HAL}$ displayed the best efficacy. Moreover, the macrophage subpopulation distribution and the secretion levels of typical cytokines were evaluated. As shown in Fig. 4G, benefiting from the combinatorial anti-inflammatory effect of NABM and HAL, the administration of $eNAB^{HAL}$ realized the most evidently reduced iNOS-positive population and elevated CD206-positive population. Importantly, the Western blot analysis emphasized the similar results (Fig. 4H). In the inflammation status, macrophages secreted a large number of pro-inflammatory factors, which would cause tissue damage and delay repair. After the treatment of $eNAB^{HAL}$, the secretion of pro-inflammatory factors was attenuated and the production of anti-inflammatory factors was enhanced, which is in favor of tissue repair and regeneration (Fig. 4I). However, compared with $eNAB^{HAL}$, the $eNAB^{null}$ group exhibited a mild effect on macrophages phenotype regulation to a much less extent. Collectively, these data suggested the enhanced anti-inflammatory effects of $eNAB^{HAL}$ compared with $eNAB^{null}$ attributed to the intracellular transport of HAL.

3.6. In vivo targeting and anti-inflammatory ability of $eNAB^{HAL}$

To investigate the immunoregulatory effect of $eNAB^{HAL}$ *in vivo*, the rat MI model was established by left anterior descending artery ligation to induce MI as previously reported [24]. Immunohistochemistry of acute inflammation were observed from infarcted heart sections 3 days,

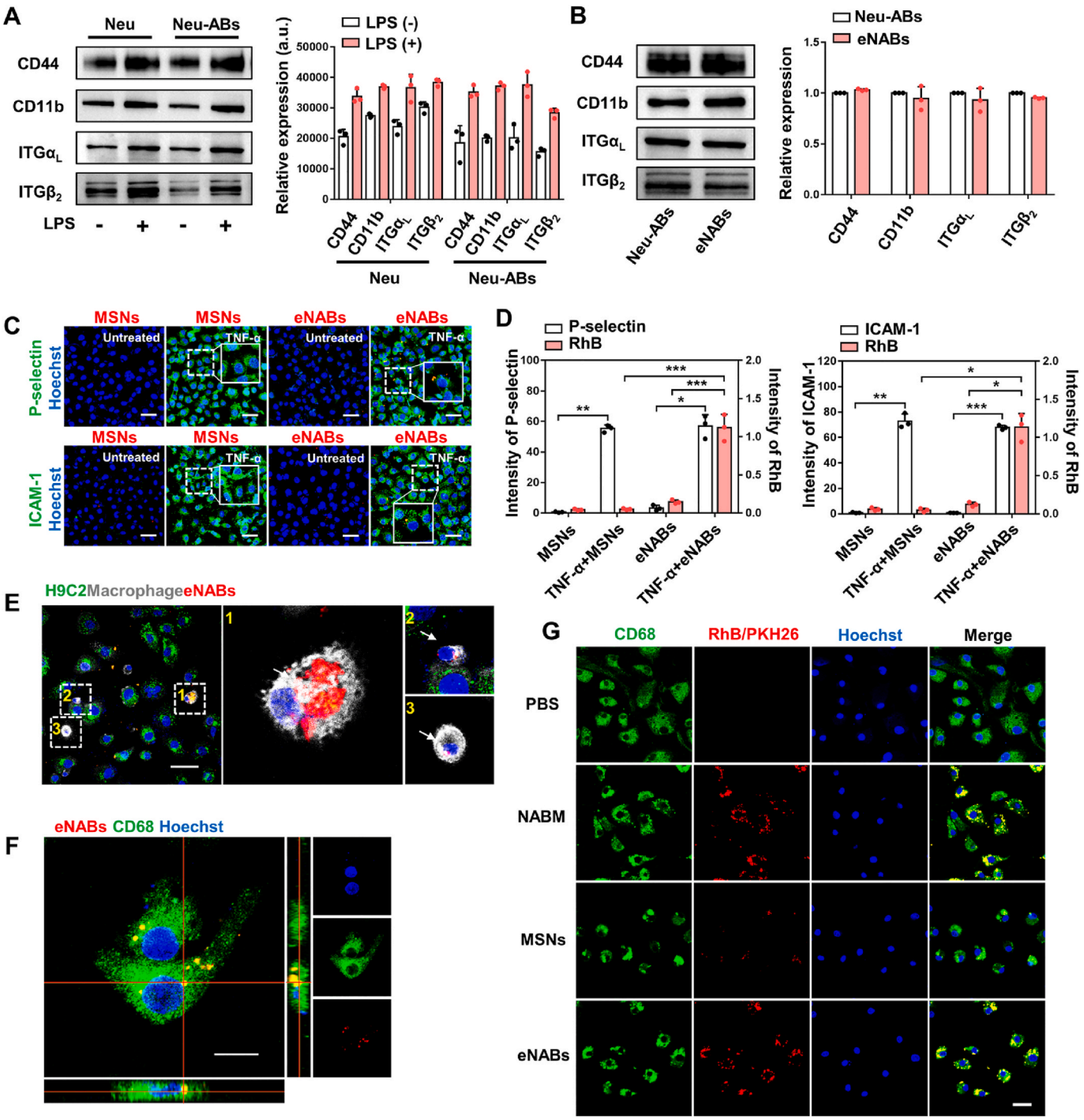

Fig. 2. Inflammation-targeting ability and cell-specific uptake of eNABs. (**A**) The expression of adhesion molecules increased in neutrophils and Neu-ABs after LPS pretreatment. (**B**) The retainment of adhesion molecules in eNABs inherited from Neu-ABs. (**C**) Representative fluorescence images showed eNABs adhered to the inflamed endothelium *in vitro*. Scale bars, 50 μm. (**D**) Quantitative analysis of the fluorescence intensity of P-selectin/ICAM-1 and MSNs/eNABs in each group (n = 3). (**E**) Representative images of eNABs (red) engulfed by macrophages (white)/cardiomyocytes (green) in a coculture pattern. The white arrows indicate eNABs engulfed by macrophages, and the right panel shows the high magnification of the representative images. Scale bar, 50 μm. (**F**) Intracellular uptake of eNABs by macrophages. Scale bar, 10 μm. (**G**) Cell-specific uptake of eNABs by macrophages. Representative fluorescence images of macrophages after different treatments. Scale bar, 20 μm. Data are presented as means ± SD. Statistical analysis was performed using one-way analysis of variance (ANOVA) for **D** (*$P < 0.05$; **$P < 0.01$; ***$P < 0.001$).

7 days post ligation by confocal microscopy (Fig. S7A). It's obvious that a shift in macrophage subtype from a major $CD206^+$ population in the normal state to a markedly increased numbers of $iNOS^+$ population at 3 days post MI, until 7 days $CD206^+$ macrophages began to expand in heart along with tremendous $iNOS^+$ macrophages. These results consistent with recent reports demonstrated that there are just slight resident macrophages in the normal heart, which are mainly $CD206^{high}$ expression. When myocardial infarction occurred, plenty of macrophages migrated and infiltrated in the infarcted zone and pro-inflammatory macrophages dominated in the early inflammatory state at days 1–3 post-MI, which followed by a resolution phase, during which macrophages are gradually polarized toward an

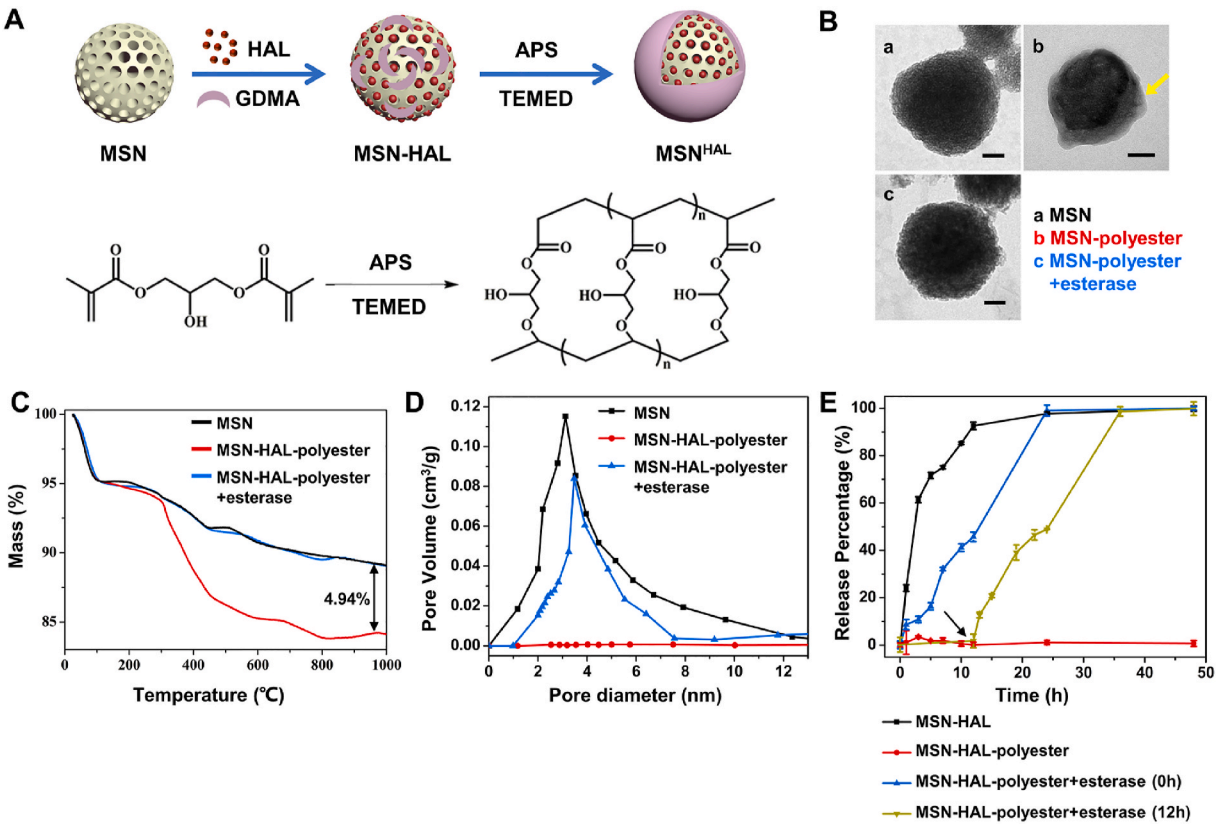

Fig. 3. Construction and characterization of HAL-loaded and polyester-capped MSNs as intelligence core for intracellular drug delivery. (**A**) Diagram of MSN functionalization and drug loading procedure. (**B**) Representative TEM images of MSN (**a**), MSN-polyester (**b**) and MSN-polyester after esterase treatment (**c**). Scale bars, 50 nm. The thermal gravity analysis (**C**) and pore-size distribution (**D**) of bare MSN, MSN-polyester, and MSN-polyester after esterase treatment. (**E**) The release curve of HAL from MSNs in different groups ($n = 3$). 0 h refers to esterase was added to MSN-HAL-polyester at the beginning, and the arrow represents esterase was added after 12 h incubation of MSN-HAL-polyester in PBS. Data are presented as means ± SD.

anti-inflammatory state at days 4–7 [2,30]. Hence, agents were injected at 3 days post MI in the *in vivo* studies.

Although the location of the infarcted myocardium in MI is difficult to achieve local application, the advantages of eNABs enable systemic treatment of the inflammatory lesion in the inaccessible region. To investigate the inflammation-targeted ability of eNAB^{HAL} *in vivo*, we detected the biodistribution and fate of administered eNAB^{HAL} in MI rat model. *Ex vivo* fluorescence imaging revealed significant accumulation of eNAB^{HAL} in infarcted zone of hearts (Fig. 5A), especially compared with PBS and MSN^{HAL} groups. It was also worthwhile to note that strong signals were observed in the lungs of MSN^{HAL}-treated animals, suggesting that nanoparticles failed to bypass the small lung vasculature bed owing to aggregation caused by low stability. These results were further validated by microscopy. The tissue fluorescence results showed increased accumulation of eNAB^{HAL} in the hearts, rather than MSN^{HAL} (Fig. 5B). Furthermore, we extended the time point to 12 h and 24 h to evaluate the *in vivo* targeting ability of eNAB^{HAL}. The results (Fig. S7B) showed that the accumulation of eNAB^{HAL} reached a peak at 12 h in heart after injection, and gradually decreased at 24 h. The targeting efficiency (Fig. S7C) calculated as the percentage of eNAB^{HAL} in heart to the total injection dose (ID) showed that the highest heart-targeting efficiency was about 8% ID. The fluorescence results (Fig. S7D) also showed that the accumulation of eNAB^{HAL} in heart was increased at 12 h compared with that at 3 h, and decreased at 24 h, which were consistent with *ex vivo* fluorescence results. Moreover, immunostaining revealed eNAB^{HAL} were mainly taken up by CD11b^{+} and CD68^{+}CD11b^{+} macrophages *in vivo* (Fig. 5C, Fig. S7E), but not His48^{+} neutrophils (Fig. S7F). To explore whether engulfment of engineered neutrophil apoptotic bodies could promote the polarization of macrophages, the expression of iNOS, CD206 and Arg1 were detected by Western blot. As shown in Fig. 5D, eNAB^{HAL}-treated rats decreased iNOS expression while increased CD206 and Arg1 expression, indicating that eNAB^{HAL} promoted the growing anti-inflammatory subpopulation and suppressed the pro-inflammatory subpopulation effectively. Furthermore, eNAB^{HAL} treatment markedly decreased the number of pro-inflammatory iNOS^{+} macrophages, and promoted that of anti-inflammatory CD206^{+} macrophages as shown by confocal analysis (Fig. 5E). The infiltration of macrophages in the border zone was further evaluated by hematoxylin and eosin (H&E) staining 2 weeks after treatment. As shown in Fig. 5F, cross sections of hearts demonstrated notably reduced inflammatory cell population at the border zone in the eNAB^{HAL} group. In addition, we also explored if the eNABs could change the infiltration of other immune cells. From the results (Fig. S8), administration of eNAB^{HAL} reduced the infiltration of neutrophils, but have little effect on T cell infiltration. Overall, these data indicated that attributable to the enhanced macrophage uptake, eNAB^{HAL} could facilitate effective transition of the inflammatory phase to the reparative phase and arrest the infiltration of inflammatory cells for better cardiac repair.

3.7. *Administration of eNAB^{HAL} improved cardiac function after MI*

To determine whether increased eNAB^{HAL} accumulation and subsequent macrophage polarization to the anti-inflammatory phenotype could further ameliorate myocardial remodeling and improve cardiac function, infarcted rats were randomly subjected to intravenous infusions of either PBS, eNAB^{null}, MSN^{HAL} or eNAB^{HAL} at 3 days after MI (Fig. 6A). At 4 weeks after treatment, Masson's trichrome staining were performed to assess the area of collagen-containing fibrous tissue, the results showed that eNABs-treated heart exhibited heart protection to some extent compared with PBS group. MSN^{HAL} did not confer any

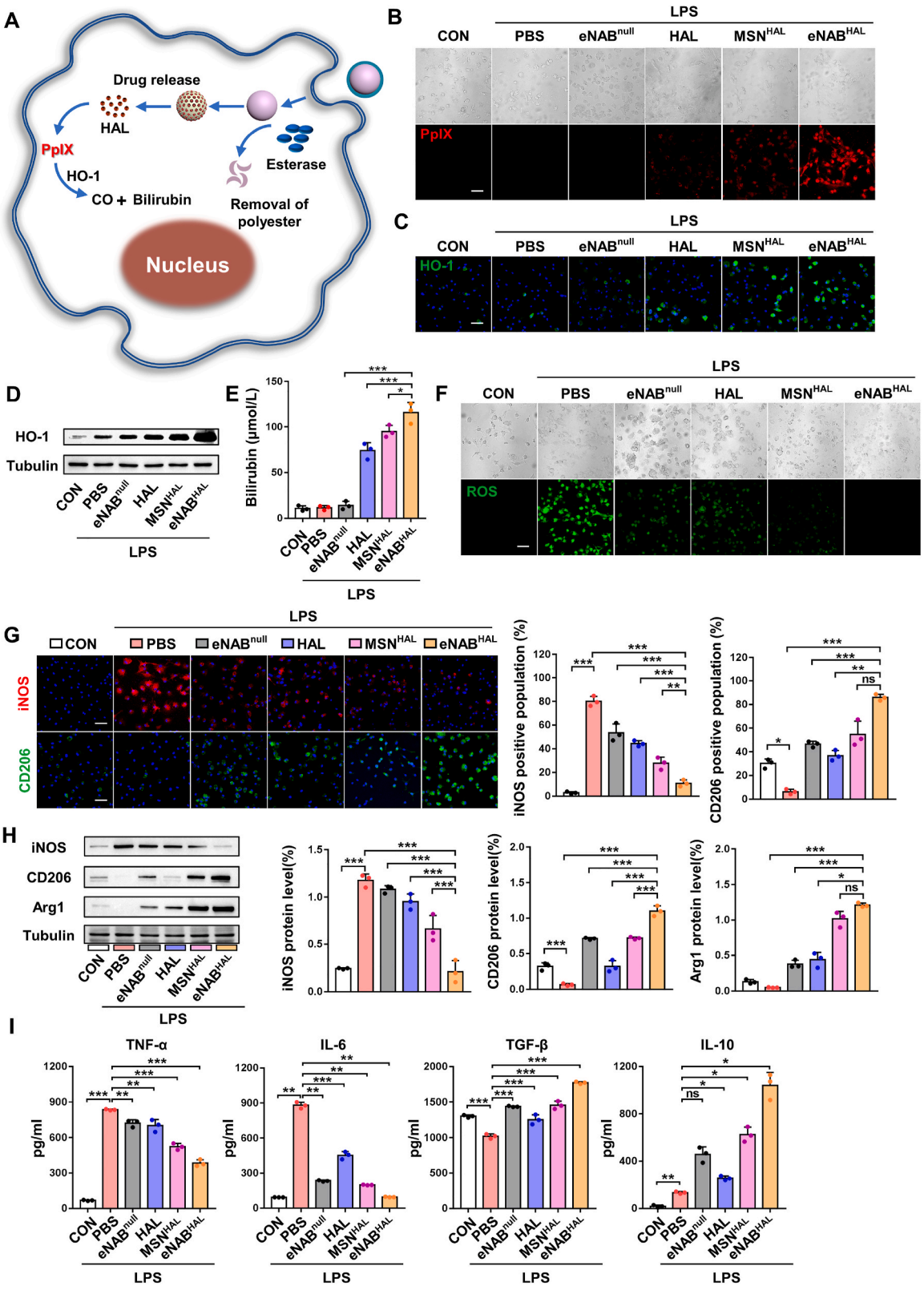

Fig. 4. Intracellular delivery of HAL and synergetic anti-inflammatory effects of eNAB^{HAL}. (**A**) Schematic illustration of the intracellular delivery of HAL and the metabolism of HAL to the anti-inflammatory products in the cytoplasma. (**B**) Representative fluorescence images of PpIX in cells after different treatments. Scale bar, 50 μm. (**C**) Representative fluorescence images of HO-1 expression in cells after different treatments. Scale bar, 50 μm. (**D**) Western blotting analysis of HO-1 expression in cells. (**E**) The secretion level of bilirubin in cells after different treatments (n = 3). (**F**) The ROS level in inflammatory macrophages after different treatments. Scale bar, 50 μm. (**G**) Representative fluorescence images of the macrophage phenotypes and the percentage of the iNOS/CD206-positive population (n = 3). Scale bars, 50 μm. (**H**) Western blotting analysis of the phenotype markers of macrophages. (**I**) Detection of the levels of immune factors in the supernatants (n = 3). Data are presented as means ± SD. Statistical analysis was performed using one-way ANOVA (ns, not significant; *$P < 0.05$; **$P < 0.01$; ***$P < 0.001$).

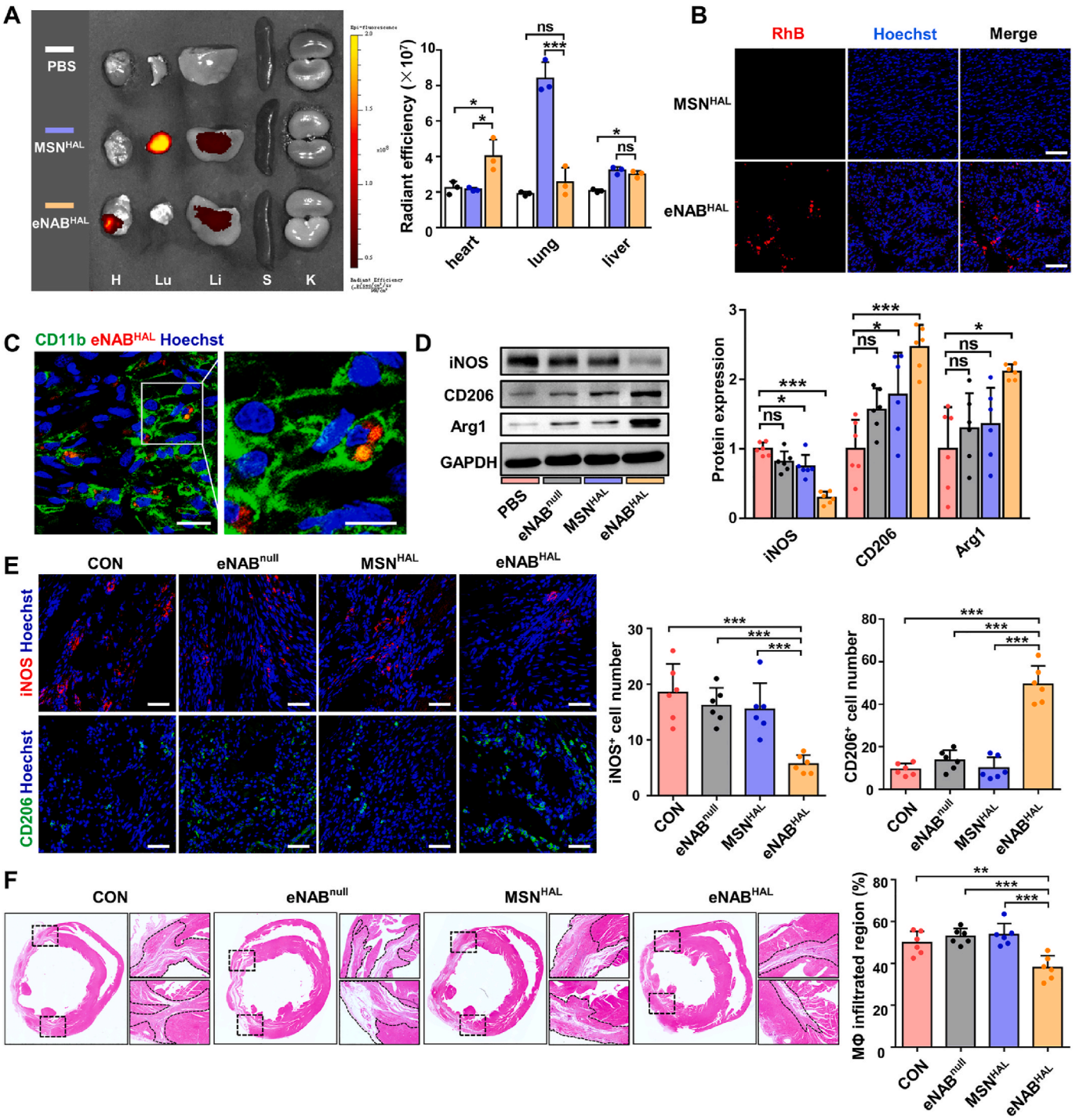

Fig. 5. *In vivo* accumulation, uptake and anti-inflammation effect of eNAB^{HAL} in MI rat model. (**A**) *Ex vivo* fluorescence imaging of the major organs 3 h after injection of DiR-labeled eNAB^{HAL} compared with PBS and MSN^{HAL} (n = 3). Quantification of average fluorescence units in organs. H, Lu, Li, S and K indicate heart, lung, liver, spleen, and kidney, respectively. The color scale corresponds to radiant efficiency [(p/sec/cm^2/sr)/(μW/cm^2)]. (**B**) Accumulation of RhB-labeled eNAB^{HAL} in heart section (n = 3). Scale bars, 100 μm. (**C**) Immunostaining revealed RhB-labeled eNAB^{HAL} could be engulfed by CD11b$^+$ macrophages *in vivo* at 3 h after injection (n = 3). The right panel (scale bar, 10 μm) represented the corresponding magnified boxed area from left panel (scale bar, 20 μm). (**D**) Western blot analysis of the phenotype markers in heart tissues from rats treated with PBS, eNAB^{null}, MSN^{HAL} or eNAB^{HAL}. (**E**) Representative fluorescence images of iNOS$^+$ and CD206$^+$ macrophages in heart from rats treated with PBS, eNAB^{null}, MSN^{HAL} or eNAB^{HAL} (n = 6). Scale bars, 50 μm. (**F**) H&E staining of the heart cross-sections and the quantitative analysis of inflammation infiltration 2 weeks after the treatment (n = 6). Data are presented as means ± SD. Statistical analysis was performed using one-way ANOVA (ns, not significant; *$P < 0.05$; **$P < 0.01$; ***$P < 0.001$).

therapeutic benefits, and injection of eNAB^{HAL} generated the most significant reduction of infarct size (Fig. 6B), which confirmed the targeted efficacy and the synergistic effect of NABM and HAL. Echocardiography studies were performed at baseline (24 h post-infarction) and endpoint (4 weeks post-injection) as an indicator of cardiac function (Fig. 6C–F). Left ventricular ejection fractions (LVEF) and left ventricular fractional shortening (LVFS) in PBS and MSN^{HAL} group deteriorated continuously, application of eNAB^{null} kept cardiac function from further deterioration.

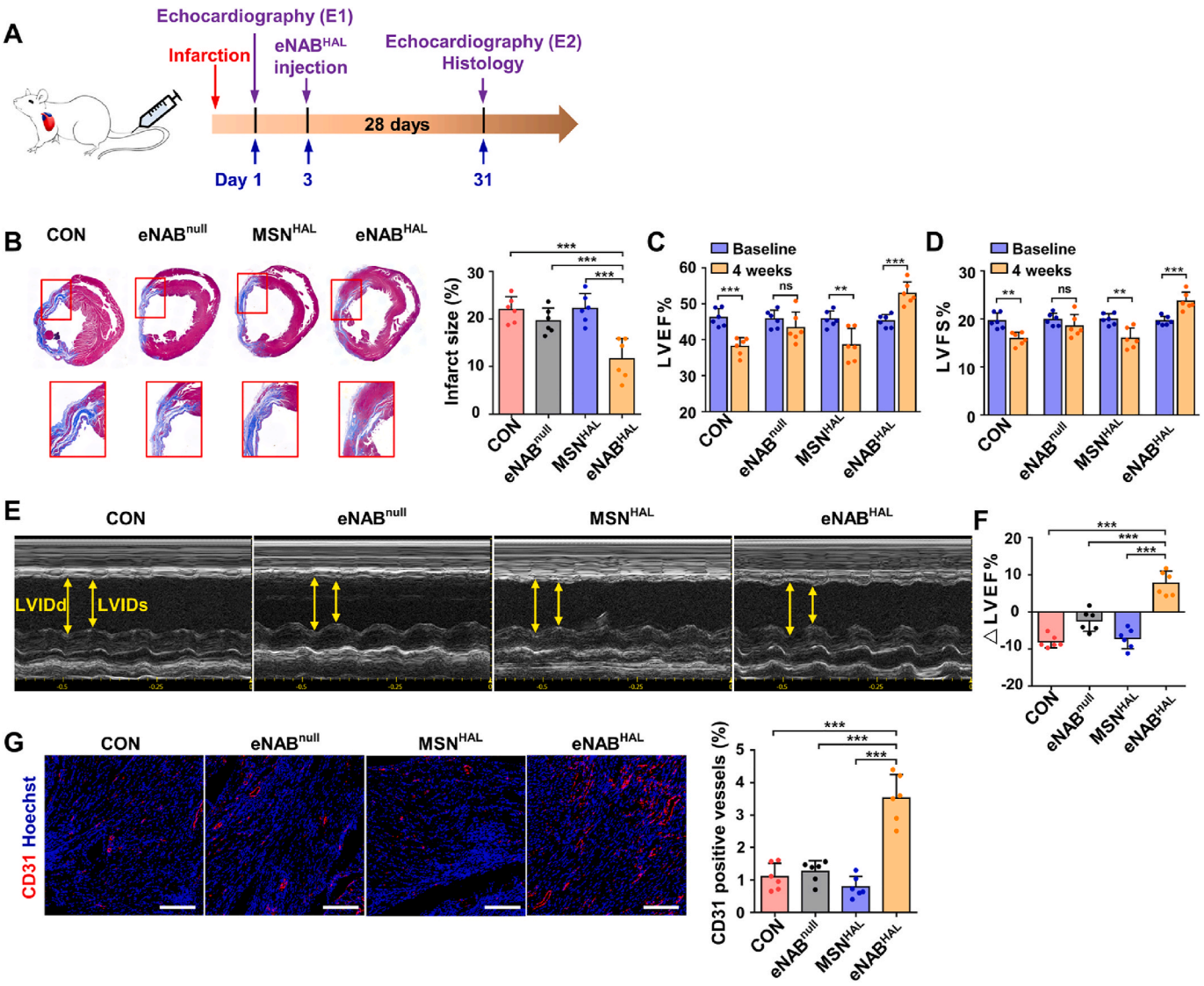

Fig. 6. Administration of eNAB^{HAL} improved cardiac function and promoted vascularization in a rat model of MI. (**A**) Treatment protocol within a MI rat model. Two echocardiography studies were performed 1 day after ligation of the left anterior descending artery (E1) and 4 weeks post treatment (E2). (**B**) Representative images of Masson's trichrome staining on heart sections from rats treated with PBS, eNAB^{null}, MSN^{HAL} or eNAB^{HAL}, the panels below showed the high magnification of the representative images. Fibrosis of infarct size was quantified. (**C**) Left ventricular ejection fraction (LVEF) in MI models at 4 weeks after treatments. (**D**) Left ventricular fractional shortening (LVFS) in MI models at 4 weeks after treatments. (**E**) Representative echocardiographic images for various groups after 4 weeks. Distance between yellow arrows indicates left ventricular internal end diastolic dimension (LVIDd) and left ventricular internal end systolic dimension (LVIDs), respectively. (**F**) Ejection fraction expressed as differences between E1 and E2 per group. (**G**) Confocal microscopic images showing eNAB^{HAL} injection boosted angiogenesis in infarction border zone at 4 weeks after treatment. Scale bars, 200 μm. Data are presented as means ± SD (n = 6). Statistical analysis was performed using unpaired two-tailed t-tests for **C** and **D**, and one-way ANOVA for **B**, **F** and **G** (ns, not significant; $^{**}P < 0.01$; $^{***}P < 0.001$).

However, only the eNAB^{HAL}-treated rats exhibited significantly improved LVEFs and LVFSs. Similarly, ΔLVEFs was calculated to clarify the effects of different treatments, and the findings are clear to show the improvement of cardiac function by eNAB^{HAL} (Fig. 6F). Neovascularization is indispensable for tissue repair and regeneration, and insufficient angiogenesis will accelerate myocardial fibrosis. Thus, regulation of cardiac remodeling was further assessed on the extent of angiogenesis, the heart sections were stained for the expression of vascular endothelial cells (CD31). Treatment of eNAB^{HAL} increased the number of CD31-positive vasculatures in the post-MI heart, especially compared with PBS groups (Fig. 6G). This may be attributed to the uptake of engineered neutrophil apoptotic bodies by macrophages and the anti-inflammatory transformation on macrophages as previously reported, which created a stable microenvironment conducive to regeneration [31]. Toxicity evaluation was also conducted in normal rats with the administration of eNAB^{null}, MSN^{HAL} or eNAB^{HAL}. Histological evaluation revealed no apparent acute organ damage in all treated groups (Fig. S9A). Serum biochemistry analyses demonstrated no significant difference in levels of alanine aminotransferase (ALT) and aspartate aminotransferase (AST) tested for hepatic function, urea nitrogen (BUN) and creatinine (Crea) for renal function, and creatine kinase (CK) for heart function among the groups (Fig. S9B). Collectively, these data suggested that eNAB^{HAL} with the enhanced immunoregulatory efficacy can be used as a safe formulation for MI therapy effectively to promote tissue regeneration.

4. Discussion

The administration of apoptotic cells as therapeutic intervention to promote tissue regeneration by immunomodulation for a wide range of

diseases has been developed for decades. The recognition and uptake of donor apoptotic cells by phagocytes within an inflammatory milieu could induce immune tolerance which in turn promote tissue regeneration [32–35]. In addition, strategies that induce apoptotic cells *in situ* in inflammatory disorders have shown potential [12,36]. However, phagocytosis of apoptotic cell debris (e.g., intracellular pathogen or inflammasome) has been shown to likely result in the subsequent infection of macrophages [37]. Moreover, the repeated administration of apoptotic cells can increase risk of autoimmunity [38]. Apoptotic bodies, a type of EVs secreted by cells undergoing apoptosis, which inherited the most properties of apoptotic cells and mediated different biological functions, have been increasingly explored as potential therapeutics [39]. We previously showed that MSC-derived ABs were protective in models of myocardial ischemia injury by maintaining tissue homeostasis [17], and modular designed chimeric ABs exhibited reinforced therapeutic potential for inflammation modulation [18]. We have now shown that the engineered neutrophil ABs recapitulate immunomodulatory activities of their parent cells by inheritance of the adhesion molecules and apoptosis-related signaling molecules. Moreover, ABs offer appealing features for therapeutic application, including stability in circulation or storage, biocompatibility and low toxicity, which highlights the superiority of cell-free therapy.

Natural EVs derived from different sources provide therapeutic benefit for the management of some intractable disorders in preclinical studies and have achieved success particularly in tissue regeneration [40,41]. Choosing an appropriate cell source for EV production according to the intended therapeutic application is of utmost importance. However, the heterogeneity and complex compositions represent major barriers for translation of naturally secreted EVs to the clinic [19]. Moreover, after systemic administration, the whole-body biodistribution profiles of EVs influences the therapeutic efficacy and toxicity. EVs secreted by most cells show limited tropism to a specific cell type [42]. Through previous exploration, we found that ABs secreted by special cells could be modified to achieve targeted functional regulation of specific immune cells at inflammatory sites [18]. At the same time, replacement of the heterogeneous contents by on-demand designed nanoparticles loaded with approved drugs is capable to circumvent the barriers to enhance the potential of EVs. What's more, the protective shield of the preloaded therapeutics supported by ABs against enzymatic degradation and immune clearance during circulation effectively enhances the lifetime and promotes the treatment efficiency, which realizes the safe and effective delivery to targeted tissue/cells. Therefore, the individual designed EVs could be widely used in treatment by change and modification of drugs, core structure and EVs type to implement modularization.

It is widely acknowledged that the adult mammalian heart has limited capacity for regeneration following injury [43]. Consequently, the reduction of myocardial damage after acute injury and early preservation of cardiac function remains one of the main clinical challenges currently. At 1–2 weeks after MI, the damaged area is mainly in the inflammatory microenvironment, and tissues undergo apoptosis and gradually develop fibrosis, which is in the critical period of inflammation and remodeling [44]. The persisted apoptotic levels until 4 weeks [45] and the high levels of inflammatory cytokines suggested a heightened state of inflammation status in the chronically ischemic heart, which hampered the repair capacity of myocardium [46]. Subsequently, in the absence of treatment, local apoptosis and inflammation continued to occur in infarcted myocardium, and the fibrosis lesions continued to expand, leading to infarct expansion, decreased LV thickness and deteriorated myocardial function in a time-dependent manner over the 4-week period [47,48], which is consistent with our results in PBS group (Fig. 6C, D, F). There is growing evidence that cardiac regenerative potential following MI closely correlates with the immune response and consequent inflammatory modulation has become a key focus of therapeutic strategy [4,49]. Recent studies which aimed at inducing resolution of inflammation have demonstrated the definite effect in improving cardiac function and promoting angiogenesis [29,50,51]. Furthermore, recent studies on EVs/engineered EVs in the treatment of MI also ascribed the therapeutic effect to the systemic modulation of inflammation and/or direct site-specific effects [15]. Therefore, it is of scientific significance and feasible to adopt immunoregulatory therapy for myocardial infarction in the early stage (within 2 weeks post-MI). Macrophages are a kind of important immune cells, which are plastic and heterogeneous according to the microenvironment. Previous studies demonstrated that pro-inflammatory macrophages dominated in the early inflammatory state (peak at day 3–4 post-MI). Followed by a resolution phase (peak at day 7 post-MI), anti-inflammatory macrophages represented the predominant subset to promote tissue repair [30]. Herein, we established a novel engineered strategy to simulate the natural repair process after acute inflammation by transient mass neutrophils apoptosis, which potentiated the impact on macrophage reprogramming to achieve an enhanced therapeutic efficacy. The good physicochemical, biological properties and outstanding immunoregulatory ability of eNABs efficiently attenuated left ventricle remodeling and promoted cardiac function recovery, which expand the known therapy strategy of cardiac regeneration using the EVs. However, the extensive application and clinical popularization of engineered vesicles will need further validation in large animal experiments, complicated disease models and larger sample sizes.

5. Conclusions

In summary, this study demonstrated the construction of engineered neutrophil apoptotic bodies *via* combining natural apoptotic body membrane and a drug carrier module to simulate the natural apoptosis and repair process after acute inflammation. The eNABs inherited the inflammation-tropism and macrophage-specific targeting ability from the natural membrane, which enhanced the accumulation of these nanovesicles in infarcted heart and the subsequent efferocytosis by macrophages *in situ* after systemic administration. The preloaded HAL was triggered to release intracellularly to further promote the macrophages reprogramming and enhance anti-inflammatory effects, which finally elicited an impressive effect on inflammatory resolution and cardiac function improvement. Taken together, the eNABs not only provide a promising alternative for the treatment of myocardial infarction, but also opens up a new avenue for engineered extracellular vesicles.

CRediT authorship contribution statement

Lili Bao: Investigation, Formal analysis, Validation, Writing – original draft. **Geng Dou:** Investigation, Formal analysis, Validation, Writing – original draft, Funding acquisition. **Ran Tian:** Investigation, Formal analysis, Writing – original draft. **Yajie Lv:** Resources. **Feng Ding:** Methodology. **Siying Liu:** Funding acquisition. **Ruifeng Zhao:** Methodology. **Lu Zhao:** Data curation. **Jun Zhou:** Funding acquisition. **Lin Weng:** Formal analysis. **Yan Dong:** Funding acquisition. **Bei Li:** Funding acquisition. **Shiyu Liu:** Writing – review & editing, Funding acquisition, Conceptualization. **Xin Chen:** Writing – review & editing, Funding acquisition. **Yan Jin:** Supervision, Resources, Funding acquisition.

Declaration of competing interest

The authors declare that they have no competing interests.

Acknowledgments

This work was supported by National Key Research and Development Program of China (2016YFC1101400), National Natural Science Foundation of China (31800817), Innovative Talent Project of Shaanxi province (2020KJXX-057), National Natural Science Foundation of

China (31870970), National Natural Science Foundation of China (81991504), Key Research and Development Program of Shaanxi Province (2019SF-073), Young Talent Support Program of Stomatology of FMMU (41741835-MZ2020D5).

Appendix A. Supplementary data

Supplementary data to this article can be found online at https://doi.org/10.1016/j.bioactmat.2021.08.008.

References

[1] G.C.o.D. Collaborators, Global, regional, and national age-sex specific mortality for 264 causes of death, 1980-2016: a systematic analysis for the Global Burden of Disease Study 2016, Lancet 390 (10100) (2017) 1151–1210.
[2] S.B. Ong, S. Hernández-Reséndiz, G.E. Crespo-Avilan, R.T. Mukhametshina, X. Y. Kwek, H.A. Cabrera-Fuentes, D.J. Hausenloy, Inflammation following acute myocardial infarction: multiple players, dynamic roles, and novel therapeutic opportunities, Pharmacol. Ther. 186 (2018) 73–87.
[3] S.A. Dick, J.A. Macklin, S. Nejat, A. Momen, X. Clemente-Casares, M.G. Althagafi, J. Chen, C. Kantores, S. Hosseinzadeh, L. Aronoff, A. Wong, R. Zaman, I. Barbu, R. Besla, K.J. Lavine, B. Razani, F. Ginhoux, M. Husain, M.I. Cybulsky, C. S. Robbins, S. Epelman, Self-renewing resident cardiac macrophages limit adverse remodeling following myocardial infarction, Nat. Immunol. 20 (1) (2019) 29–39.
[4] M. Horckmans, L. Ring, J. Duchene, D. Santovito, M.J. Schloss, M. Drechsler, C. Weber, O. Soehnlein, S. Steffens, Neutrophils orchestrate post-myocardial infarction healing by polarizing macrophages towards a reparative phenotype, Eur. Heart J. 38 (3) (2017) 187–197.
[5] M.C. Greenlee-Wacker, Clearance of apoptotic neutrophils and resolution of inflammation, Immunol. Rev. 273 (1) (2016) 357–370.
[6] E. Wan, X.Y. Yeap, S. Dehn, R. Terry, M. Novak, S. Zhang, S. Iwata, X. Han, S. Homma, K. Drosatos, J. Lomasney, D.M. Engman, S.D. Miller, D.E. Vaughan, J. P. Morrow, R. Kishore, E.B. Thorp, Enhanced efferocytosis of apoptotic cardiomyocytes through myeloid-epithelial-reproductive tyrosine kinase links acute inflammation resolution to cardiac repair after infarction, Circ. Res. 113 (8) (2013) 1004–1012.
[7] K. Shirakawa, J. Endo, M. Kataoka, Y. Katsumata, N. Yoshida, T. Yamamoto, S. Isobe, H. Moriyama, S. Goto, H. Kitakata, T. Hiraide, K. Fukuda, M. Sano, IL (Interleukin)-10-STAT3-Galectin-3 Axis is essential for osteopontin-producing reparative macrophage polarization after myocardial infarction, Circulation 138 (18) (2018) 2021–2035.
[8] J. Dalli, L.V. Norling, D. Renshaw, D. Cooper, K.Y. Leung, M. Perretti, Annexin 1 mediates the rapid anti-inflammatory effects of neutrophil-derived microparticles, Blood 112 (6) (2008) 2512–2519.
[9] M. Perretti, N. Chiang, M. La, I.M. Fierro, S. Marullo, S.J. Getting, E. Solito, C. N. Serhan, Endogenous lipid- and peptide-derived anti-inflammatory pathways generated with glucocorticoid and aspirin treatment activate the lipoxin A4 receptor, Nat. Med. 8 (11) (2002) 1296–1302.
[10] X.J. Li, D.P. Liu, H.L. Chen, X.H. Pan, Q.Y. Kong, Q.F. Pang, Lactoferrin protects against lipopolysaccharide-induced acute lung injury in mice, Int. Immunopharm. 12 (2) (2012) 460–464.
[11] U. Sydlik, H. Peuschel, A. Paunel-Görgülü, S. Keymel, U. Krämer, A. Weissenberg, M. Kroker, S. Seghrouchni, C. Heiss, J. Windolf, A. Bilstein, M. Kelm, J. Krutmann, K. Unfried, Recovery of neutrophil apoptosis by ectoine: a new strategy against lung inflammation, Eur. Respir. J. 41 (2) (2013) 433–442.
[12] A.G. Rossi, D.A. Sawatzky, A. Walker, C. Ward, T.A. Sheldrake, N.A. Riley, A. Caldicott, M. Martinez-Losa, T.R. Walker, R. Duffin, M. Gray, E. Crescenzi, M. C. Martin, H.J. Brady, J.S. Savill, I. Dransfield, C. Haslett, Cyclin-dependent kinase inhibitors enhance the resolution of inflammation by promoting inflammatory cell apoptosis, Nat. Med. 12 (9) (2006) 1056–1064.
[13] A. Ortega-Gomez, M. Perretti, O. Soehnlein, Resolution of inflammation: an integrated view, EMBO Mol. Med. 5 (5) (2013) 661–674.
[14] N. Pallet, M. Dieudé, J. Cailhier, M. Hébert, The molecular legacy of apoptosis in transplantation, Am. J. Transplant. 12 (6) (2012) 1378–1384.
[15] C. Pezzana, F. Agnely, A. Bochot, J. Siepmann, P. Menasché, Extracellular vesicles and biomaterial design: new therapies for cardiac repair, Trends Mol. Med. 27 (3) (2021) 231–247.
[16] D. Liu, X. Kou, C. Chen, S. Liu, Y. Liu, W. Yu, T. Yu, R. Yang, R. Wang, Y. Zhou, S. Shi, Circulating apoptotic bodies maintain mesenchymal stem cell homeostasis and ameliorate osteopenia via transferring multiple cellular factors, Cell Res. 28 (9) (2018) 918–933.
[17] H. Liu, S. Liu, X. Qiu, X. Yang, L. Bao, F. Pu, X. Liu, C. Li, K. Xuan, J. Zhou, Z. Deng, S. Liu, Y. Jin, Donor MSCs release apoptotic bodies to improve myocardial infarction via autophagy regulation in recipient cells, Autophagy 16 (12) (2020) 2140–2155.
[18] G. Dou, R. Tian, X. Liu, P. Yuan, Q. Ye, J. Liu, S. Liu, J. Zhou, Z. Deng, X. Chen, S. Liu, Y. Jin, Chimeric apoptotic bodies functionalized with natural membrane and modular delivery system for inflammation modulation, Sci. Adv. 6 (30) (2020), eaba2987.
[19] R.C. de Abreu, H. Fernandes, P.A. da Costa Martins, S. Sahoo, C. Emanueli, L. Ferreira, Native and bioengineered extracellular vesicles for cardiovascular therapeutics, Nat. Rev. Cardiol. 17 (11) (2020) 685–697.
[20] A. Esmaeili, S. Hosseini, M. Baghaban Eslaminejad, Engineered-extracellular vesicles as an optimistic tool for microRNA delivery for osteoarthritis treatment, Cell. Mol. Life Sci. 78 (1) (2021) 79–91.
[21] X. Xu, Z. Huo, J. Guo, H. Liu, X. Qi, Z. Wu, Micromotor-derived composites for biomedicine delivery and other related purposes, Bio-des. Manuf. (3) (2020) 133–147.
[22] G. Wu, J. Zhang, Q. Zhao, W. Zhuang, J. Ding, C. Zhang, H. Gao, D.W. Pang, K. Pu, H.Y. Xie, Molecularly engineered macrophage-derived exosomes with inflammation tropism and intrinsic heme biosynthesis for atherosclerosis treatment, Angew Chem. Int. Ed. Engl. 59 (10) (2020) 4068–4074.
[23] X. Chen, A.H. Soeriyadi, X. Lu, S.M. Sagnella, M. Kavallaris, J.J. Gooding, Dual bioresponsive mesoporous silica nanocarrier as an "AND" logic gate for targeted drug delivery cancer cells, Adv. Funct. Mater. 24 (44) (2014) 6999–7006.
[24] Q. Liu, T. Hu, L. He, X. Huang, X. Tian, H. Zhang, L. He, W. Pu, L. Zhang, H. Sun, J. Fang, Y. Yu, S. Duan, C. Hu, L. Hui, H. Zhang, T. Quertermous, Q. Xu, K. Red-Horse, J.D. Wythe, B. Zhou, Genetic targeting of sprouting angiogenesis using Apln-CreER, Nat. Commun. 6 (2015) 6020.
[25] T.T. Tang, L.L. Lv, B. Wang, J.Y. Cao, Y. Feng, Z.L. Li, M. Wu, F.M. Wang, Y. Wen, L.T. Zhou, H.F. Ni, P.S. Chen, N. Gu, S.D. Crowley, B.C. Liu, Employing macrophage-derived microvesicle for kidney-targeted delivery of dexamethasone: an efficient therapeutic strategy against renal inflammation and fibrosis, Theranostics 9 (16) (2019) 4740–4755.
[26] R. Li, Y. He, Y. Zhu, L. Jiang, S. Zhang, J. Qin, Q. Wu, W. Dai, S. Shen, Z. Pang, J. Wang, Route to rheumatoid arthritis by macrophage-derived microvesicle-coated nanoparticles, Nano Lett. 19 (1) (2019) 124–134.
[27] N. Hannemann, S. Cao, D. Eriksson, A. Schnelzer, J. Jordan, M. Eberhardt, U. Schleicher, J. Rech, A. Ramming, S. Uebe, A. Ekici, J.D. Canete, X. Chen, T. Bauerle, J. Vera, C. Bogdan, G. Schett, A. Bozec, Transcription factor Fra-1 targets arginase-1 to enhance macrophage-mediated inflammation in arthritis, J. Clin. Invest. 129 (7) (2019) 2669–2684.
[28] W. Jiang, L. Ma, X. Xu, One-dimensional microstructure-assisted intradermal and intracellular delivery, Bio-des. Manuf. 2 (1) (2019) 24–30.
[29] J. Han, Y.S. Kim, M.Y. Lim, H.Y. Kim, S. Kong, M. Kang, Y.W. Choo, J.H. Jun, S. Ryu, H.Y. Jeong, J. Park, G.J. Jeong, J.C. Lee, G.H. Eom, Y. Ahn, B.S. Kim, Dual roles of graphene oxide to attenuate inflammation and elicit timely polarization of macrophage phenotypes for cardiac repair, ACS Nano 12 (2) (2018) 1959–1977.
[30] S.D. Prabhu, N.G. Frangogiannis, The biological basis for cardiac repair after myocardial infarction: from inflammation to fibrosis, Circ. Res. 119 (1) (2016) 91–112.
[31] J. Li, Y. Song, J.Y. Jin, G.H. Li, Y.Z. Guo, H.Y. Yi, J.R. Zhang, Y.J. Lu, J.L. Zhang, C. Y. Li, C. Gao, L. Yang, F. Fu, F.L. Chen, S.M. Zhang, M. Jia, G.X. Zheng, J.M. Pei, L. H. Chen, CD226 deletion improves post-infarction healing via modulating macrophage polarization in mice, Theranostics 10 (5) (2020) 2422–2435.
[32] D. El Kebir, L. József, W. Pan, L. Wang, N.A. Petasis, C.N. Serhan, J.G. Filep, 15-epi-lipoxin A4 inhibits myeloperoxidase signaling and enhances resolution of acute lung injury, Am. J. Respir. Crit. Care Med. 180 (4) (2009) 311–319.
[33] M. Gray, K. Miles, D. Salter, D. Gray, J. Savill, Apoptotic cells protect mice from autoimmune inflammation by the induction of regulatory B cells, Proc. Natl. Acad. Sci. U. S. A. 104 (35) (2007) 14080–14085.
[34] M. Lichtenauer, M. Mildner, A. Baumgartner, M. Hasun, G. Werba, L. Beer, P. Altmann, G. Roth, M. Gyöngyösi, B.K. Podesser, H.J. Ankersmit, Intravenous and intramyocardial injection of apoptotic white blood cell suspensions prevents ventricular remodelling by increasing elastin expression in cardiac scar tissue after myocardial infarction, Basic Res. Cardiol. 106 (4) (2011) 645–655.
[35] P. Szodoray, G. Papp, B. Nakken, M. Harangi, M. Zeher, The molecular and clinical rationale of extracorporeal photochemotherapy in autoimmune diseases, malignancies and transplantation, Autoimmun. Rev. 9 (6) (2010) 459–464.
[36] E.E. McGrath, H.M. Marriott, A. Lawrie, S.E. Francis, I. Sabroe, S.A. Renshaw, D. H. Dockrell, M.K. Whyte, TNF-related apoptosis-inducing ligand (TRAIL) regulates inflammatory neutrophil apoptosis and enhances resolution of inflammation, J. Leukoc. Biol. 90 (5) (2011) 855–865.
[37] I.K. Poon, C.D. Lucas, A.G. Rossi, K.S. Ravichandran, Apoptotic cell clearance: basic biology and therapeutic potential, Nat. Rev. Immunol. 14 (3) (2014) 166–180.
[38] D. Mevorach, J.L. Zhou, X. Song, K.B. Elkon, Systemic exposure to irradiated apoptotic cells induces autoantibody production, J. Exp. Med. 188 (2) (1998) 387–392.
[39] S. Caruso, I.K.H. Poon, Apoptotic cell-derived extracellular vesicles: more than just debris, Front. Immunol. 9 (2018) 1486.
[40] O.P.B. Wiklander, M. Brennan, J. Lötvall, X.O. Breakefield, S. El Andaloussi, Advances in therapeutic applications of extracellular vesicles, Sci. Transl. Med. 11 (492) (2019).
[41] S. Sahoo, M. Adamiak, P. Mathiyalagan, F. Kenneweg, S. Kafert-Kasting, T. Thum, Therapeutic and diagnostic translation of extracellular vesicles in cardiovascular diseases: roadmap to the clinic, Circulation 143 (14) (2021) 1426–1449.
[42] L. Barile, G. Vassalli, Exosomes: therapy delivery tools and biomarkers of diseases, Pharmacol. Ther. 174 (2017) 63–78.
[43] E. Tzahor, K.D. Poss, Cardiac regeneration strategies: staying young at heart, Science 356 (6342) (2017) 1035–1039.
[44] X. Wang, Z. Guo, Z. Ding, J.L. Mehta, Inflammation, autophagy, and apoptosis after myocardial infarction, Journal of the American Heart Association 7 (9) (2018).
[45] H.F. Weisman, B. Healy, Myocardial infarct expansion, infarct extension, and reinfarction: pathophysiologic concepts, Prog. Cardiovasc. Dis. 30 (2) (1987) 73–110.
[46] P. Uusimaa, J. Risteli, M. Niemelä, J. Lumme, M. Ikäheimo, A. Jounela, K. Peuhkurinen, Collagen scar formation after acute myocardial infarction:

relationships to infarct size, left ventricular function, and coronary artery patency, Circulation 96 (8) (1997) 2565–2572.
[47] M.P. Boyle, H.F. Weisman, Limitation of infarct expansion and ventricular remodeling by late reperfusion. Study of time course and mechanism in a rat model, Circulation 88 (6) (1993) 2872–2883.
[48] J.S. Hochman, B.H. Bulkley, Expansion of acute myocardial infarction: an experimental study, Circulation 65 (7) (1982) 1446–1450.
[49] M. Coggins, A. Rosenzweig, The fire within: cardiac inflammatory signaling in health and disease, Circ. Res. 110 (1) (2012) 116–125.
[50] T. Harel-Adar, T. Ben Mordechai, Y. Amsalem, M.S. Feinberg, J. Leor, S. Cohen, Modulation of cardiac macrophages by phosphatidylserine-presenting liposomes improves infarct repair, Proc. Natl. Acad. Sci. U. S. A. 108 (5) (2011) 1827–1832.
[51] T. Bejerano, S. Etzion, S. Elyagon, Y. Etzion, S. Cohen, Nanoparticle delivery of miRNA-21 mimic to cardiac macrophages improves myocardial remodeling after myocardial infarction, Nano Lett. 18 (9) (2018) 5885–5891.